Anharmonic organic cation vibrations in the hybrid lead halide perovskite CH₃NH₃PbI₃

Kunie Ishioka [1,*] Terumasa Tadano [1] Masatoshi Yanagida [2] Yasuhiro Shirai [2] and Kenjiro Miyano [2]

[1]*National Institute for Materials Science, Sengen 1-2-1, Tsukuba 305-0047, Japan*

[2]*National Institute for Materials Science, Namiki 1-1, Tsukuba 305-0044, Japan*

Ultrafast vibrational dynamics of inorganic-organic hybrid lead halide perovskite $CH_3NH_3PbI_3$ in the room-temperature tetragonal phase is investigated under weak photoexcitation at the band edge. Time-resolved optical Kerr effect signals exhibit periodic modulations at 4 and 8 THz due to the libration and twisting of the methylammonium molecule, in addition to the inorganic sublattice deformation at 1.2 THz. These oscillations are heavily damped and resemble the short-lived ground-state oscillation reported in a recent THz-pump study [Z. Liu *et al.*, Phys. Rev. B **101**, 115125 (2020)]. The vibrational frequencies exhibit blueshifts with increasing pump fluence, contrary to the expectation from conventional laser heating. Our *ab initio* lattice dynamics simulations reveal strongly anharmonic vibrational potentials for the zone-center optical phonon modes, and thereby confirm the anharmonicity to be the origin of the experimentally observed frequency blueshifts.

I. INTRODUCTION

Organic-inorganic hybrid lead halide perovskites such as methylammonium lead iodide ($CH_3NH_3PbI_3$ or $MAPbI_3$) have attracted great attention in the past few years not only because of their excellent performances in solar cells and other optoelectronic applications, but also because of their unusual physical properties [1,2]. The material consists of the heavy inorganic lead halide octahedral framework (e.g., PbI_3) and the light organic group (e.g., CH_3NH_3 or methylammonium MA) embedded in them. The structural and electronic properties of the hybrid perovskites are essentially similar to those of the all-inorganic counterpart such as $CsPbI_3$. The conduction band minimum and the valence band maximum of both materials consist primarily of Pb and halogen orbitals [3]. The inorganic framework is mechanically soft, and the low-frequency phonons at the Brillouin zone boundaries involving large-amplitude halogen atom motions exhibit strong anharmonicity [2,4–12]. This leads to mechanical instability involving structural phase transition with temperature [11,13], dynamic structural fluctuation on picosecond timescale [8,14,15], and low thermal conductivity [5]. A number of experimental and theoretical studies suggested that the inorganic lattice is deformed around a charge carrier to form a polaron, which arguably contributes to the long carrier lifetime and diffusion length of lead halide perovskites [16–23].

The roles of the organic molecules in defining the material and optoelectronic properties are less straightforward and have been under extensive debate. Theoretical studies predicted that the larger size of the organic cations (e.g., MA^+) and their stronger interactions with the inorganic framework lead to the stabilization of the highly anharmonic PbI_3 sublattice [3,7,8,24] in comparison with inorganic cations

(e.g., Cs^+). There have been experimental and theoretical indications that the rotation of the MA^+ cations within the inorganic cage is restricted in the room-temperature tetragonal phase of $MAPbI_3$, whereas the cations rotate freely in the high-temperature cubic phase and the rotation is frozen in the low-temperature orthorhombic phase [13,15,25–27]. The rotational rearrangement of the organic cations was proposed to play an important role in the charge screening and the polaron formation [18,28–32].

The atomic vibrations (phonons) and their coupling with electronic states in the hybrid perovskites have been studied extensively by means of Raman scattering spectroscopy [11,15,24,33–38], inelastic neutron scattering [6,12,39], and THz spectroscopy [20,40,41]. Whereas distinct phonon peaks were observed in the low-temperature phase, at room temperature the vibrational spectra typically consisted of weak broad bands, especially in the low-frequency region where the vibrations of the inorganic cages and those of the rigid organic molecules appear [11,12,39–41]. This is because the static spectroscopic techniques detect the temporal average of the inorganic lattice and cation motions that fluctuate on a picosecond timescale.

An alternative approach to experimentally investigate the phonons is to excite coherent vibrations with an ultrashort optical pulse and detect them as periodic modulations of optical properties in a pump-probe scheme. Time-resolved experimental studies have been performed on hybrid lead halide perovskites under electronically resonant [19,32,42–47] and nonresonant [23,45,48–50] excitation conditions. Resonant excitation with visible pump light can provide insights on the interaction of Raman-active optical phonons at the Brillouin zone center with high-density photoexcited carriers. Coherent oscillation modes ranging from 0.6 to 5 THz were reported for tetragonal $MAPbI_3$ at room temperature [19,32,42–44,46]. A recent two-dimensional (2D) electronic spectroscopic study [32] observed a delayed rise (~0.7 ps) and relatively long lifetime (>2 ps) of the MA libration at 5 THz and interpreted

———————
*ishioka.kunie@nims.go.jp

it as the coherent oscillation *after* the polaron formation. Nonresonant excitation with infrared (IR) pump, by contrast, can offer dynamic information on the IR-active zone-center phonons in the absence of photocarriers [23,47–50]. A recent THz-pump experiment [23] revealed a considerably shorter lifetime (<1 ps) for the MA restricted rotation at ∼5 THz. The apparent contrast in the MA cation dynamics between the resonant and nonresonant experiments suggests a qualitative difference between the electron-phonon couplings on the electronic excited and ground states. Because the visible and IR pump lights can, in principle, excite different phonon modes, however, direct comparison between the two types of experiments is not necessarily straightforward.

In the present study, we investigate the Raman-active phonons of MAPbI$_3$ in the room-temperature tetragonal phase under weak photoexcitation at the band edge. By using a broadband near-infrared pump pulse whose central energy is slightly below the band gap, we aim at a preresonant excitation condition with a minimal photocarrier density. Periodic modulations by short-lived coherent MA molecular twisting and libration are clearly detected in the time-resolved optical Kerr effect (TR-OKE) signals, together with that by PbI$_6$ octahedral deformation. Their heavy dampings are consistent with the ground-state oscillation dynamics reported in the earlier nonresonant study. The good signal-to-noise (S/N) ratio of our signals allows quantitative analyses, which indicates the strong vibrational anharmonicities. Our theoretical simulations on the zone-center optical phonon modes in tetragonal MAPbI$_3$ confirm our mode assignments and the strong vibrational anharmonicity for both organic and inorganic vibrational modes.

II. EXPERIMENTAL METHODS

The sample consists of a 1-mm-thick glass substrate, a 250-nm-thick MAPbI$_3$ film fabricated by a two-step spin coating procedure [51,52], and a 100-nm-thick polymethyl methacrylate (PMMA) capping layer to keep off the atmospheric humidity and oxygen. Details of the preparation and characterization of the MAPbI$_3$ samples are described in Sec. I of the Supplemental Material (SM) [53].

TR-OKE measurements are performed under ambient conditions using the setup schematically illustrated in Fig. 1(a) (see SM [53]). Pump-induced anisotropy in the transmissivity, $\Delta T_y - \Delta T_x$, is detected, which we hereafter refer to as the TR-OKE signal, while the time delay t between the pump and probe pulses is scanned continuously at 20 Hz (fast scan). The light source for the TR-OKE measurements is an output of a Ti:sapphire oscillator with 12-fs duration and 80-MHz repetition rate. The laser spectrum is centered at wavelength of 810 nm (photon energy of 1.53 eV) and has a full width of 130 nm (0.24 eV), as shown in Fig. 1(b). Only a small fraction (∼1/6) of the spectrum exceeds the nominal band gap of MAPbI$_3$, 1.6 eV at room temperature, and thereby offers a preresonant excitation condition. The maximum pump fluence employed in the present study, 57 μJ/cm^2, corresponds to the incident photon flux of $F = 2.3 \times 10^{14}$ photons/cm^2, and the upper limit for the photoexcited carrier density is estimated to be 3×10^{17} cm^{-3}. This density is higher by two orders of magnitude than the chemically doped carrier concentration
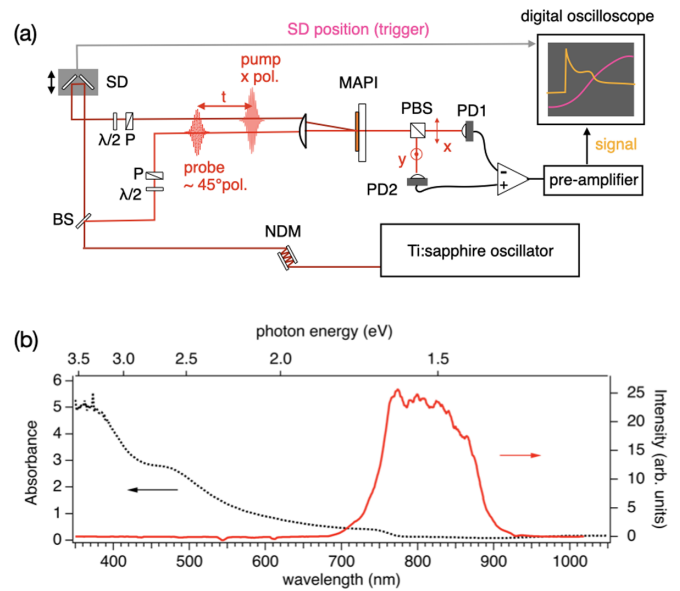

FIG. 1. (a) Schematic illustration of the time-resolved optical Kerr effect (TR-OKE) measurement setup. NDM: negative dispersion mirror pair; BS: beam splitter; SD: fast-scan delay stage; $\lambda/2$: half-wave plate; P: polarizer; MAPI: MAPbI$_3$ sample; PBS: polarizing beam splitter; PD1 and PD2: photodetectors. (b) Spectrum of the laser pulse employed in the pump-probe measurements (red solid curve, plotted against the right axis) compared with the absorbance of MAPbI$_3$ film (black dotted curve, plotted against the left axis).

[52], but is still lower by one to two orders of magnitude than those employed in the previous visible-pump studies [32,43,46]. We confirm that no irreversible photodamage is done on the sample by measuring the same spot from the lowest to the highest fluences and then again at the lowest.

III. EXPERIMENTAL RESULTS

Figure 2(a) plots the as-measured TR-OKE signal of the MAPbI$_3$ film. The signals exhibit a sharp (<100 fs) bipolar spike at $t = 0$, followed by a positive baseline that hardly decays within the present time window of ∼10 ps. The initial spike can be interpreted as the pump-induced polarizations in the PbI$_6$ octahedral framework and among the MA$^+$ cations, both of which are expected to relax on a timescale of a few-hundred femtoseconds [14,25–27]. The following positive baseline indicates the long-lived photoexcited carrier population at the band edge, which relaxes on a nanosecond or longer timescale [31,54,55].

On top of this nonoscillatory response, a much weaker quasiperiodic modulation is also detected. Figure 2(b) shows the oscillatory component after subtraction of the nonoscillatory baseline obtained at different pump fluences. The fast Fourier transform (FFT) spectrum in Fig. 2(c) shows that the coherent response is dominated by two modes at ∼4 and 8 THz (∼130 and 260 cm^{-1}). In addition, we find a weaker FT peak at 1.2 THz (40 cm^{-1}).

The frequency of 1.2 THz is close to that reported by the previous pump-probe [19,46,48] and Raman [11] studies. This mode was attributed to I-Pb-I angular bending within the *ab* plane based on the theoretical calculations
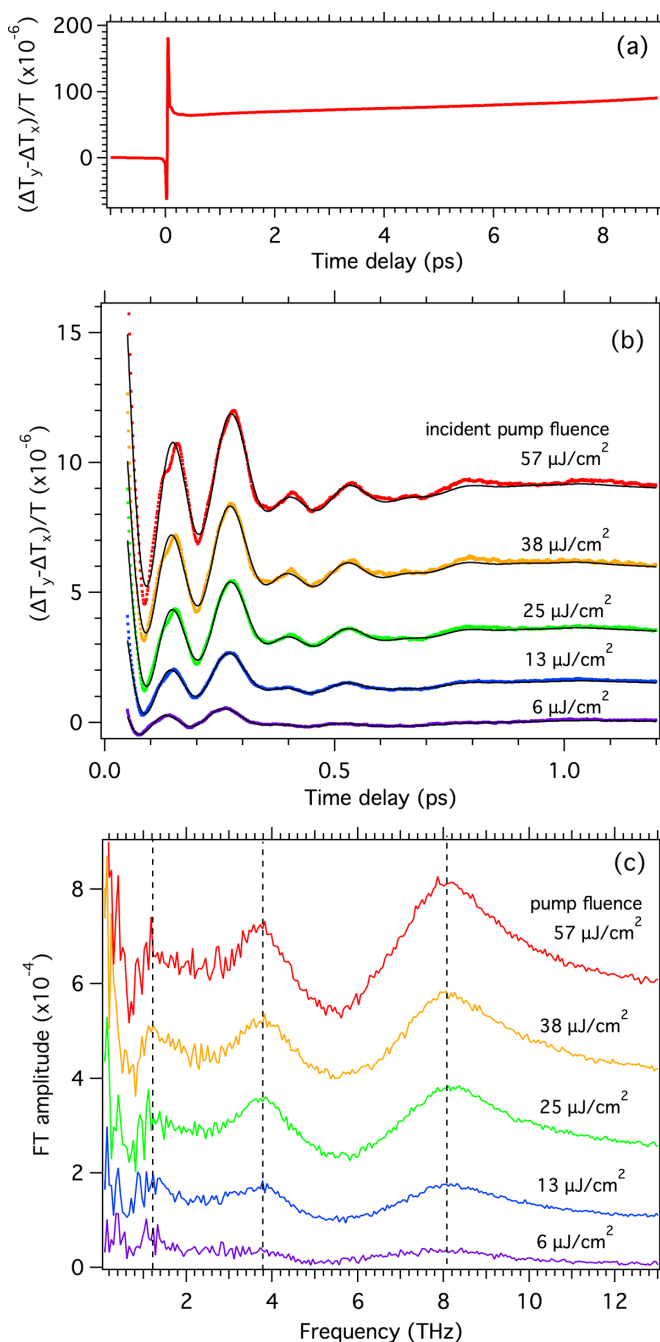
FIG. 2. (a) As-measured TR-OKE signal of $MAPbI_3$ at incident pump fluence of 32 $\mu J/cm^2$. (b) Oscillatory components of the TR-OKE signals pumped at different pump fluences (colored dots) and fits to a triple damped harmonic function (black curves). (c) Fast Fourier transform (FFT) spectra of (b). Vertical broken lines indicate the approximate positions of the FT peaks. Traces in (b) and (c) are offset for clarity.

[4,19,36,37,39,56,57]. The 4-THz mode was also previously observed in both time-resolved [32,43,45] and Raman studies [4,18,24,36,37,56–59] and assigned as the libration of the rigid MA^+ molecule. The 8-THz mode has so far been reported only by Raman studies [4,24,34,36,39,56,59] and assigned as the intramolecular hindered rotation of CH_3 against NH_3. We hereafter refer to this mode as the MA twisting,

though it was called differently (e.g., torsion or disrotatory motion) in the literature. The MA cations are coupled with the surrounding PbI_3 cage via ion-ion, hydrogen bonding, and ion-dipole interactions, which gives rise to the restoring force for both the molecular twisting and librational motions.

We note that the MA libration and twisting modes are also observed in the Raman spectrum of the same sample (see SM [53]). In the TR-OKE signal of a single crystal $MAPbI_3$ (see SM [53]), however, the MA oscillations are not so distinct. This is primarily because of the poorer heat dissipation for the ~500-μm-thick freestanding single crystal, in comparison with the thin polycrystalline film on the substrate, and therefore a lower threshold for laser-induced damage (~6 $\mu J/cm^2$). For this reason, we cannot gain a sufficient S/N ratio to observe the weak signal from the MA motions. Below the damage threshold, the TR-OKE signal of the single crystal is dominated by a relatively long-lived oscillation at 1.5 THz (50 cm^{-1}) due to the PbI_3 deformation.

To extract quantitative information from the phonon dynamics of the $MAPbI_3$ thin film, we analyze the coherent oscillations by fitting to a triple damped harmonic function,

$$
\begin{aligned}
f_t(t) = {} & A_b \exp(-\Gamma_b t) \sin(\omega_b t + \phi_b) \\
& + A_l \exp(-\Gamma_l t) \sin(\omega_l t + \phi_l) \\
& + A_t \exp(-\Gamma_t t) \sin(\omega_t t + \phi_t),
\end{aligned} \tag{1}
$$

with the subscripts b, l, and t denoting the Pb-I angular bending, the MA^+ libration, and the MA^+ twisting, respectively. In Fig. 2(a), we see that the fits (black curves) satisfactorily reproduce the experimental data (colored dots) for $t \gtrsim 60$ fs. Here we see no significant delayed rise in the MA oscillation amplitudes, in apparent contrast to the previous visible-pump study [32]. Also, the dephasings of the MA oscillations are much faster ($\Gamma^{-1} = 0.1$–0.2 ps) in the present study, as shown in Fig. 3(b), compared with the long-lasting excited state vibration in the previous study. The heavily damped MA oscillations rather resemble the MA libration reported in the THz-pump study [23].

Figure 3 summarizes the fitting parameters as a function of pump fluence. The amplitudes [Fig. 3(a)] of all three vibrational modes increase slightly sublinearly with pump fluence, indicating that the coherent vibrations are induced via a one-photon process. The dephasing rates [Fig. 3(b)] are nearly independent of pump fluence, supporting that the effects of the photocarriers and the laser-induced lattice heating on the dephasing are small.

Most notably, the frequencies [Fig. 3(c)] exhibit blueshifts with increasing pump fluence until they reach saturations at ~20 $\mu J/cm^2$. Such blueshift, or bond stiffening, with increasing pump fluence is in contrast to the typical frequency redshift, or bond softening, due to laser-induced lattice and electronic heating. Instead, it can, in principle, be explained by considering a highly anharmonic vibrational potential, whose slope becomes steeper and energy spacing becomes larger at larger atomic coordinate.

Previous theoretical studies predicted a highly anharmonic vibrational potential for the Pb-I bending modes at the Brillouin zone boundaries for $MAPbI_3$ in the high-temperature cubic phase [5,6,8]. A similarly highly anharmonic vibrational potential was also predicted for the MA
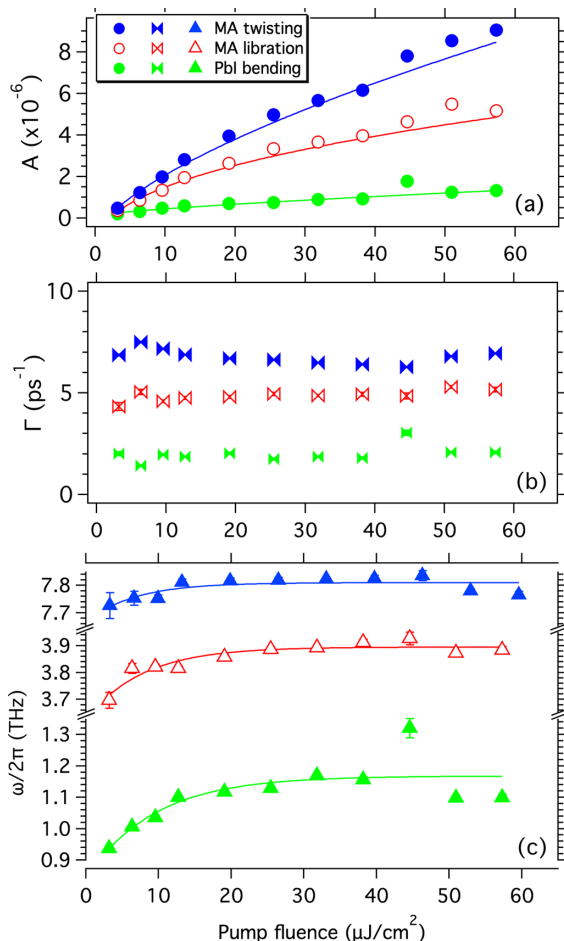
FIG. 3. (a) Initial amplitudes, (b) dephasing rates, and (c) frequencies, obtained from fitting the oscillatory TR-OKE signals to a triple damped harmonic function, as a function of incident pump fluence. Curves are to guide the eye.

spinning, i.e., rotations of the NH_3 and CH_3 groups in the same direction, in the low-temperature orthorhombic phase of $MAPbI_3$ [60]. Information for the zone-center phonons of $MAPbI_3$ in the room-temperature tetragonal phase, which could be directly compared with our experimental observations, has been very limited [9,10], however.

In principle, the fitting to Eq. (1) also gives the initial phase ϕ, which is often used to distinguish the generation mechanism (impulsive stimulated Raman scattering or displacive excitation) of the coherent phonons in opaque solids [61]. The initial phases obtained from the fitting (see SM [53]) take values between $\phi = 0$ and $\pi/2$ (sine and cosine functions of time) that are strongly dependent on the pump fluence. The MA libration and twisting are each a cosine function of time at the lowest fluence and deviate from it with increasing fluence, whereas the Pb bending approaches a sine function at high fluences.

On one hand, the theoretical model of coherent phonon generation in semimetals [61] predicted the initial phase to depend on the relaxation time of the photoexcited carriers. According to this modeling, the oscillation is a sine (cosine) function of time when the carrier relaxes sufficiently fast (slow) compared with the oscillation period, and takes

an intermediate phase when the carrier relaxation and the oscillation occur on the similar timescale (see SM [53]). The initial phases obtained from the fitting can therefore be an indication of the fluence-dependent carrier relaxation time in the range of 10–100 fs. This timescale corresponds to the very early stage of photoexcited carrier dynamics, e.g., the thermalization of free carriers [43,62] and the carrier cooling near the band edge [17]. On the other hand, the damped harmonic function [Eq. (1)] is not necessarily appropriate to describe an oscillation in an anharmonic potential, whose frequency can be time dependent. With the TR-OKE signals for the first 100 fs being obscured by an intense carrier response, it is extremely difficult to quantitatively analyze the time dependence of the frequencies for the heavily damped oscillations in the present study, leaving much ambiguity in the determination of the initial phases.

IV. THEORETICAL SIMULATIONS

To gain a deeper understanding of the zone-center optical phonons of tetragonal $MAPbI_3$, we performed an *ab initio* lattice dynamics simulation based on density functional theory (DFT). The DFT calculations were conducted using the Vienna *ab initio* simulation package (VASP) [63], which implemented the projector augmented wave (PAW) method [64,65]. The experimental lattice constants of tetragonal $MAPbI_3$ at 300 K reported in Ref. [66] were employed. As for the internal coordinates, we employed the low-energy structure of Ref. [67] as a starting point and then relaxed the coordinates by DFT until the forces acting on atoms became less than 0.5 meV/Å. For comparison, we also performed phonon calculations with the theoretical lattice constants obtained from DFT. The results (see SM [53]) are very similar to those presented below, except that the phonon frequencies are systematically higher due to the smaller unit-cell volume. A kinetic energy cutoff of 500 eV and the $4 \times 4 \times 3$ Monkhorst-Pack $\boldsymbol{k}$ points were employed. For the exchange-correlation potential, we employed the PBEsol functional [68] since it has better prediction accuracy of the lattice constants than local-density approximation (LDA) or the Perdew–Burke–Ernzerhof (PBE) functional. The harmonic phonon calculation was performed using the finite displacement method, as implemented in the ALAMODE code [69].

While the tetragonal phase is realized only in the temperature range of 161–330 K, the harmonic phonon theory predicts this phase to be dynamically stable even at $T = 0$ K, in accord with previous theoretical calculations. Figure 4(a) shows the phonon dispersion and the atom-projected phonon density of states (DOS) of tetragonal $MAPbI_3$ calculated with a $2 \times 2 \times 2$ supercell in the low-frequency region below 350 cm^{-1}. In this frequency range, 76 normal modes are found at the Γ point of the Brillouin zone. Hereafter, we index the normal modes in the ascending order of their frequencies ω_ν calculated within the harmonic approximation, as shown with blue bars in Fig. 5(a). For each normal mode, we decompose the displacements of the atoms into the translations, rotations, and internal vibrations of the PbI_6 octahedra and MA molecules, based on the approach reported in Ref. [56]. Unlike Ref. [56], however, we also consider the twisting motion of MA (see SM [53]). The result, shown in Fig. 4(b), indicates
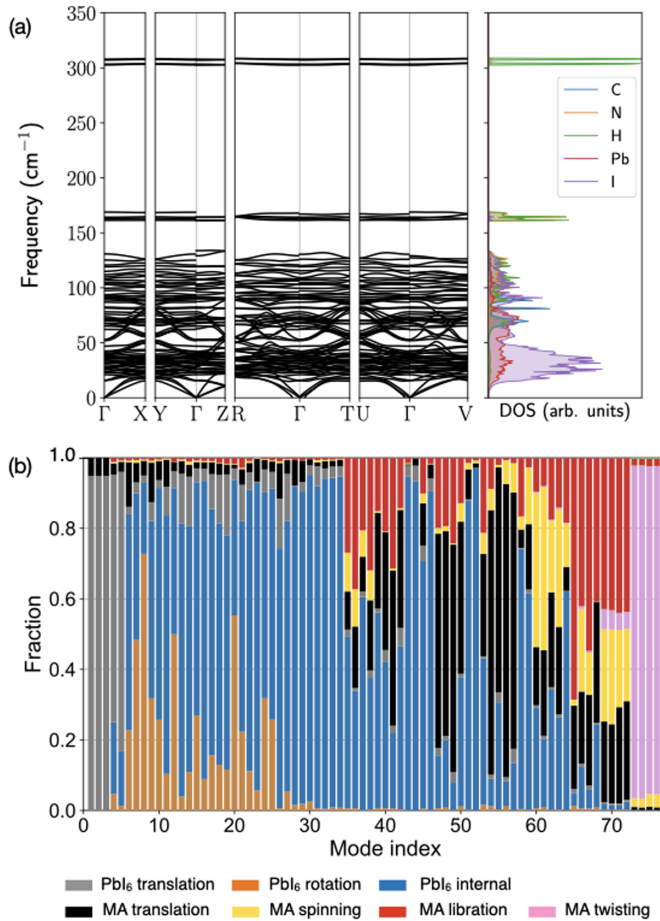
FIG. 4. (a) Calculated harmonic phonon dispersion curves along the high-symmetry points (left panel) and the atom-projected phonon DOS (right panel) of tetragonal MAPbI$_3$ in the low-frequency region. (b) Decomposition of the zone-center phonons of tetragonal MAPbI$_3$ into inorganic and organic vibrational components. The height of each colored stick represents the fractional contribution of the vibrational component. Phonon modes are indexed in the ascending order of the harmonic frequencies.

that modes $\nu = 1$–3 are pure PbI$_6$ translation (acoustic phonons). Modes $\nu = 4$–35 ($\omega_\nu \lesssim 65$ cm^{-1}) are dominated by the PbI$_6$ rotation and stretching. Modes $\nu = 36$–72 ($\omega_\nu = 66$–165 cm^{-1}) are mixtures of the PbI$_6$ internal motions with the MA translation, libration, and spinning. Modes $\nu = 73$–76 ($\omega_\nu \simeq 300$ cm^{-1}) are contributed almost exclusively by the MA twisting.

In the present experiment, where the TR-OKE signals show short-lived oscillations that are similar to the previously reported ground-state oscillations, we expect that coherent phonons are excited predominantly via impulsive stimulated Raman scattering (ISRS) [70]. The detection of the coherent phonons in the transmission geometry also requires the phonon mode to have nonzero Raman polarizability [71]. We therefore evaluate the Raman scattering intensity of the normal modes to help assign the experimentally observed phonon modes (see SM [53]). This is done by first calculating the dielectric constant tensor component ϵ_{jk}^∞ as a function of the normal coordinate displacement Q_ν based on density functional perturbation theory. The Raman polarizability tensor

component a_{jk}^ν is then evaluated as [72,73]

$$a_{jk}^\nu = \frac{V_0}{4\pi}\frac{\partial \epsilon_{jk}^\infty}{\partial Q_\nu} \approx \frac{V_0}{4\pi}\frac{\epsilon_{jk}^\infty(+\Delta Q_\nu) - \epsilon_{jk}^\infty(-\Delta Q_\nu)}{2\Delta Q_\nu}, \quad (2)$$

where V_0 is the unit-cell volume, and ΔQ_ν is a small change in the normal coordinate displacement. Finally, the Raman scattering intensity averaged over crystallographic axes, I_{Raman}^ν, is calculated from a_{jk} [72] to compare with our experiments on microcrystals with random orientations. Figure 5(b) summarizes the I_{Raman}^ν for the 73 optical phonon modes. While most of the phonon modes are Raman active due to the low symmetry ($P1$) of the crystal structure, the Raman polarizability is particularly large ($\gtrsim 50$ Å^{4}u^{-1}) for modes $\nu = 7$, 14, 20, 25, 28, 29, 63, 65, 67, 73, and 75. The result of our harmonic phonon calculation agrees well with that of the previous theoretical prediction based on the similar harmonic model [36]. We also calculate the Raman spectrum as a function of frequency ω by taking the sum of I_{Raman}^ν convoluted with a Lorentzian function with a finite linewidth Γ over all the normal modes ν (see SM [53]). The result is shown in Fig. 5(c).

We now evaluate the anharmonicity of the vibrational potential of each phonon mode at the Γ point. We employ the self-consistent phonon (SCP) theory [74], which has successfully been applied to compute anharmonic phonon frequencies of strongly anharmonic materials [75–78]. We first calculate the potential energy surface (PES) of phonon mode ν as a function of atomic displacement Q_ν. The calculated PES is then fitted to the polynomial,

$$U(Q_\nu) - U(0) = \frac{1}{2}\omega_\nu^2 Q_\nu^2 + \sum_{k=3}^{m}\frac{1}{k!}\Phi_\nu^{(k)}Q_\nu^k, \quad (3)$$

with ω_ν^2 being the squared harmonic frequency, to obtain the anharmonic coefficients of the kth order, $\Phi_\nu^{(k)}$. Finally, the anharmonic frequency Ω_ν is obtained by solving the one-dimensional SCP equation,

$$\Omega_\nu^2 = \omega_\nu^2 + \sum_{k=1}^{n}\frac{1}{2^k k!}\Phi_\nu^{(2k+2)} \times \left[\frac{2N(\Omega_\nu, T) + 1}{2\Omega_\nu}\right]^k. \quad (4)$$

Here, $N(\Omega_\nu, T)$ denotes the Bose-Einstein distribution function at phonon frequency Ω_ν and temperature T, which is related with the normal coordinate amplitude Q_ν as

$$\langle Q_\nu^2(T)\rangle = \frac{\hbar}{2\Omega_\nu}[2N(\Omega_\nu, T) + 1]. \quad (5)$$

In the present study, we consider anharmonic terms up to the sixth order ($m = 6, n = 2$), which is sufficient to reach convergence of Ω_ν. Figure 5(d) compares the calculated anharmonic and harmonic PES for a few representative modes with relatively large Raman intensities. (See SM [53] for the PES for other selected modes.) Here the horizontal scale is set from $-Q_{\text{max},\nu}$ to $Q_{\text{max},\nu}$, where

$$Q_{\text{max},\nu} \equiv 4\sqrt{\langle Q_\nu^2(T = 300 \text{ K})\rangle} \quad (6)$$

is four times the root mean square of the displacement Q_ν at room temperature calculated with the harmonic frequency ω_ν. We find that the anharmonic PESs have higher energy than the harmonic ones at large Q for all the 73 phonon modes investigated. This leads to the higher anharmonic frequencies
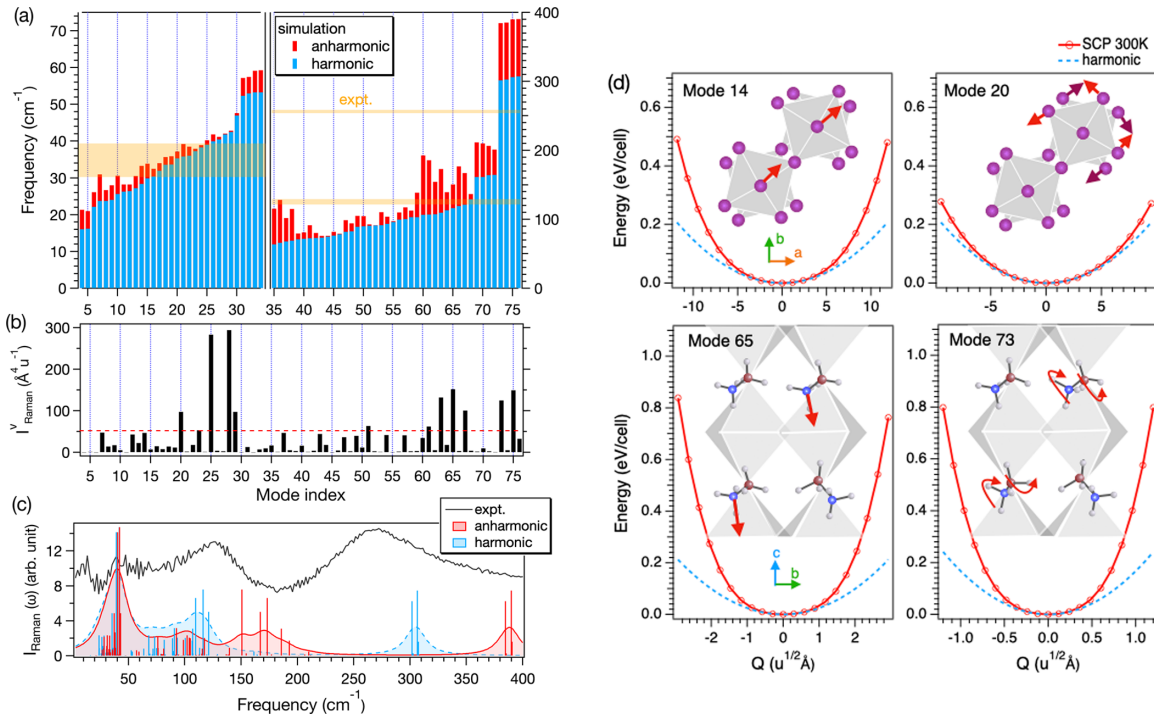
FIG. 5. (a) Phonon frequencies calculated with harmonic approximation (blue bars) and SCP theory assuming a temperature of 300 K (red bars). The horizontal yellow bands indicate the frequency ranges observed experimentally. (b) Raman polarizability $I_{Raman,\nu}$ averaged over the crystallographic axes. The dashed line corresponds to $I_{Raman}^{\nu} = 50$ Å^{4}u^{-1}. (c) Raman spectra calculated with the linewidth $\Gamma = 10$ cm^{-1}. Curves with red and blue shades denote the spectra calculated with anharmonic and harmonic frequencies. Red and blue vertical bars indicate the anharmonic and harmonic I_{Raman}^{ν}. The gray curve shows the experimental FT spectrum for the MAPbI$_3$ film, which is offset for clarity. (d) Potential energy surface (PES) of selected Raman-active phonon modes. Red solid curves represent the anharmonic PES, whereas the blue dotted lines are the PES within the harmonic approximation. The range of the horizontal axis is set from $-Q_{max,\nu}$ to $Q_{max,\nu}$ for each panel. Insets show schematic illustrations of atomic motions.

[red bars in Fig. 5(a)] than the harmonic ones (blue bars in the figure). The calculated Raman spectrum is also modified by taking into account the anharmonic effect, as shown in Fig. 5(c).

V. DISCUSSION

A comparison between the experimental results with the theoretical simulations enables us to specify the atomic motions corresponding to the coherent phonons and discuss their vibrational anharmonicities. We associate the experimental 8-THz mode to the simulated modes $\nu = 73$ and 75, which have higher frequencies than the experiment but relatively large Raman intensities ($\gtrsim 50$ Å^4 u^{-1}). Their atomic motions involve, almost exclusively, MA twisting. The overestimation in the simulated twisting frequencies may be attributed to the approximations that we have employed in our calculations, such as neglecting the intermode coupling. The experimental 4-THz mode can be related to the modes $\nu = 63$, 65, and 67 in the simulation, whose anharmonic and harmonic frequencies lie around 120–130 cm^{-1} (3.6–3.9 THz). Modes $\nu = 65$ and 67 are contributed mostly by the MA libration; mode $\nu = 63$ is a mixture of MA libration, spinning, and PbI$_6$ internal vibrations. The experimental 1.2-THz mode can be related to the modes $\nu = 14$, 20, 25, 28, and 29 in the simulation, whose frequencies lie between 30 and 50 cm^{-1} (0.9 and 1.5 THz).

These modes are mixtures of the PbI$_6$ internal vibrations (angular bendings) and rotations. Our simulations thus confirm the tentative vibrational assignments we employed in Sec. III.

The calculated PESs for the phonon modes mentioned above (see also SM [53]) reveal strong vibrational anharmonicity, except for $\nu = 28$ and 29. The anharmonicity of each phonon mode can also be inferred from the difference between the harmonic and the SCP frequencies shown in Fig. 5(a). Our theoretical results support that the strong vibrational anharmonicity is the origin of the experimental frequency blueshift at larger vibrational amplitude, as well as of the extremely fast dephasing of the zone-center phonons. In our simulation, the spinning, libration, and twisting of the organic molecules exhibit particularly strong anharmonicity in this order. The strong anharmonicity for the spinning is in line with the previous theoretical study on orthorhombic MAPbI$_3$ [60]. For the inorganic vibrations, modes $\nu = 14$, 20, and 25, which show stronger anharmonicity than $\nu = 28$ and 29, are contributed more by the PbI$_6$ rotation. This suggests that the rotational motions are responsible for the anharmonicity of the inorganic sublattice.

In the present simulation, we have neglected the effect of the photocarriers altogether. This assumption is justified by the resemblance of the short-lived oscillations observed in the present study to the ground-state oscillations reported in the

previous THz-pump study [23]. The experimentally obtained initial phases also suggest, though with a large ambiguity, that the oscillations for $t > 100$ fs are taking place after the photocarriers are relaxed to the band edge. In the present weak excitation limit, these photocarriers do not much affect the anharmonic PES of the inorganic sublattice and the organic cations. The situation would change drastically if the photocarrier density were increased by a few orders of magnitude, however. The long-living excited-state oscillations in the previous visible-pump studies [32,46] hint at reduced vibrational anharmonicity as a consequence of the stronger interaction of the charge carriers with the inorganic and organic components of the lead halide perovskite, including the polaron formation.

VI. CONCLUSION

We have experimentally and theoretically investigated the zone-center optical phonons of tetragonal MAPbI$_3$ upon pre-resonant photoexcitation. Experimental TR-OKE signals were dominated by heavily damped vibrations of the libration and twisting of the organic cations, in evident contrast to the long-lived cation vibration reported by a previous resonant experiment. We found the vibrational frequencies to be blueshifted with increasing pump fluence. Our DFT calculations on the PESs have confirmed that the blueshifts are an experimental manifestation of the strong vibrational anharmonicity. We thus successfully revealed the intrinsic dynamics of the Raman-active phonon modes of MAPb$_3$ at the weak excitation limit where the coupling to photocarriers can be neglected.

[1] D. A. Egger, A. Bera, D. Cahen, G. Hodes, T. Kirchartz, L. Kronik, R. Lovrincic, A. M. Rappe, D. R. Reichman, and O. Yaffe, Adv. Mater. **30**, 1800691 (2018).

[2] C. Katan, A. D. Mohite, and J. Even, Nat. Mater. **17**, 377 (2018).

[3] W. W. Gao, X. Gao, T. A. Abtew, Y. Y. Sun, S. B. Zhang, and P. H. Zhang, Phys. Rev. B **93**, 085202 (2016).

[4] F. Brivio, J. M. Frost, J. M. Skelton, A. J. Jackson, O. J. Weber, M. T. Weller, A. R. Goni, A. M. A. Leguy, P. R. F. Barnes, and A. Walsh, Phys. Rev. B **92**, 144308 (2015).

[5] L. D. Whalley, J. M. Skelton, J. M. Frost, and A. Walsh, Phys. Rev. B **94**, 220301(R) (2016).

[6] A. N. Beecher, O. E. Semonin, J. M. Skelton, J. M. Frost, M. W. Terban, H. Zhai, A. Alatas, J. S. Owen, A. Walsh, and S. J. L. Billinge, ACS Energy Lett. **1**, 880 (2016).

[7] L. Z. Tan, F. Zheng, and A. M. Rappe, ACS Energy Lett. **2**, 937 (2017).

[8] M. A. Carignano, S. A. Aravindh, I. S. Roqan, J. Even, and C. Katan, J. Phys. Chem. C **121**, 20729 (2017).

[9] A. Marronnier, H. Lee, B. Geffroy, J. Even, Y. Bonnassieux, and G. Roma, J. Phys. Chem. Lett. **8**, 2659 (2017).

[10] T. A. Tyson, W. Gao, Y. S. Chen, S. Ghose, and Y. Yan, Sci. Rep. **7**, 9401 (2017).

[11] R. Sharma, Z. Dai, L. Gao, T. M. Brenner, L. Yadgarov, J. Zhang, Y. Rakita, R. Korobko, A. M. Rappe, and O. Yaffe, Phys. Rev. Mater. **4**, 092401(R) (2020).

[12] A. C. Ferreira, S. Paofai, A. Letoublon, J. Ollivier, S. Raymond, B. Hehlen, B. Ruffle, S. Cordier, C. Katan, J. Even, and P. Bourges, Commun. Phys. **3**, 48 (2020).

[13] P. S. Whitfield, N. Herron, W. E. Guise, K. Page, Y. Q. Cheng, I. Milas, and M. K. Crawford, Sci. Rep. **6**, 35685 (2016).

[14] O. Yaffe, Y. Guo, L. Z. Tan, D. A. Egger, T. Hull, C. C. Stoumpos, F. Zheng, T. F. Heinz, L. Kronik, M. G. Kanatzidis, J. S. Owen, A. M. Rappe, M. A. Pimenta, and L. E. Brus, Phys. Rev. Lett. **118**, 136001 (2017).

[15] Y. Guo, O. Yaffe, D. W. Paley, A. N. Beecher, T. D. Hull, G. Szpak, J. S. Owen, L. E. Brus, and M. A. Pimenta, Phys. Rev. Mater. **1**, 042401(R) (2017).

[16] K. Miyata, T. L. Atallah, and X.-Y. Zhu, Sci. Adv. **3**, e1701469 (2017).

[17] S. A. Bretschneider, I. Ivanov, H. I. Wang, K. Miyata, X. Zhu, and M. Bonn, Adv. Mater. **30**, 1707312 (2018).

[18] M. Schlipf, S. Ponce, and F. Giustino, Phys. Rev. Lett. **121**, 086402 (2018).

[19] M. Park, A. J. Neukirch, S. E. Reyes-Lillo, M. Lai, S. R. Ellis, D. Dietze, J. B. Neaton, P. Yang, S. Tretiak, and R. A. Mathies, Nat. Commun. **9**, 2525 (2018).

[20] Y. Lan, B. J. Dringoli, D. A. Valverde-Chavez, C. S. Ponseca, M. Sutton, Y. He, M. G. Kanatzidis, and D. G. Cooke, Sci. Adv. **5**, eaaw5558 (2019).

[21] D. Ghosh, E. Welch, A. J. Neukirch, A. Zakhidov, and S. Tretiak, J. Phys. Chem. Lett. **11**, 3271 (2020).

[22] M. Puppin, S. Polishchuk, N. Colonna, A. Crepaldi, D. N. Dirin, O. Nazarenko, R. De Gennaro, G. Gatti, S. Roth, T. Barillot, L. Poletto, R. P. Xian, L. Rettig, M. Wolf, R. Ernstorfer, M. V. Kovalenko, N. Marzari, M. Grioni, and M. Chergui, Phys. Rev. Lett. **124**, 206402 (2020).

[23] Z. Liu, C. Vaswani, L. Luo, D. Cheng, X. Yang, X. Zhao, Y. Yao, Z. Song, R. Brenes, R. J. H. Kim, J. Jean, V. Bulovic, Y. Yan, K. M. Ho, and J. Wang, Phys. Rev. B **101**, 115125 (2020).

[24] C. Quarti, E. Mosconi, and F. De Angelis, Chem. Mater. **26**, 6557 (2014).

[25] A. A. Bakulin, O. Selig, H. J. Bakker, Y. L. A. Rezus, C. Müller, T. Glaser, R. Lovrincic, Z. Sun, Z. Chen, A. Walsh, J. M. Frost, and T. L. C. Jansen, J. Phys. Chem. Lett. **6**, 3663 (2015).

[26] O. Selig, A. Sadhanala, C. Müller, R. Lovrincic, Z. Chen, Y. L. A. Rezus, J. M. Frost, T. L. C. Jansen, and A. A. Bakulin, J. Am. Chem. Soc. **139**, 4068 (2017).

[27] G. M. Bernard, R. E. Wasylishen, C. I. Ratcliffe, V. Terskikh, Q. Wu, J. M. Buriak, and T. Hauger, J. Phys. Chem. A **122**, 1560 (2018).

[28] A. M. A. Leguy, J. M. Frost, A. P. McMahon, V. G. Sakai, W. Kockelmann, C. Law, X. Li, F. Foglia, A. Walsh, B. C.

O'Regan, J. Nelson, J. T. Cabral, and P. R. F. Barnes, Nat. Commun. **6**, 7124 (2015).

[29] K. T. Munson, J. R. Swartzfager, and J. B. Asbury, ACS Energy Lett. **4**, 1888 (2019).

[30] K. T. Munson, G. S. Doucette, E. R. Kennehan, J. R. Swartzfager, and J. B. Asbury, J. Phys. Chem. C **123**, 7061 (2019).

[31] P. P. Joshi, S. F. Maehrlein, and X. Y. Zhu, Adv. Mater. **31**, 1803054 (2019).

[32] H. G. Duan, V. Tiwari, A. Jha, G. R. Berdiyorov, A. Akimov, O. Vendrell, P. K. Nayak, H. J. Snaith, M. Thorwart, Z. Li, M. E. Madjet, and R. J. D. Miller, J. Am. Chem. Soc. **142**, 16569 (2020).

[33] T. Glaser, C. Müller, M. Sendner, C. Krekeler, O. E. Semonin, T. D. Hull, O. Yaffe, J. S. Owen, W. Kowalsky, A. Pucci, and R. Lovrincic, J. Phys. Chem. Lett. **6**, 2913 (2015).

[34] R. G. Niemann, A. G. Kontos, D. Palles, E. I. Kamitsos, A. Kaltzoglou, F. Brivio, P. Falaras, and P. J. Cameron, J. Phys. Chem. C **120**, 2509 (2016).

[35] L. Q. Xie, T. Y. Zhang, L. Chen, N. J. Guo, Y. Wang, G. K. Liu, J. R. Wang, J. Z. Zhou, J. W. Yan, Y. X. Zhao, B. W. Mao, and Z. Q. Tian, Phys. Chem. Chem. Phys. **18**, 18112 (2016).

[36] A. M. A. Leguy, A. R. Goni, J. M. Frost, J. Skelton, F. Brivio, X. Rodriguez-Martinez, O. J. Weber, A. Pallipurath, M. I. Alonso, M. Campoy-Quiles, M. T. Weller, J. Nelson, A. Walsh, and P. R. F. Barnes, Phys. Chem. Chem. Phys. **18**, 27051 (2016).

[37] M. A. Perez-Osorio, Q. Lin, R. T. Phillips, R. L. Milot, L. M. Herz, M. B. Johnston, and F. Giustino, J. Phys. Chem. C **122**, 21703 (2018).

[38] R. Sharma, M. Menahem, Z. B. Dai, L. Y. Gao, T. M. Brenner, L. Yadgarov, J. H. Zhang, Y. Rakita, R. Korobko, I. Pinkas, A. M. Rappe, and O. Yaffe, Phys. Rev. Mater. **4**, 051601(R) (2020).

[39] K. Druzbicki, R. S. Pinna, S. Rudic, M. Jura, G. Gorini, and F. Fernandez-Alonso, J. Phys. Chem. Lett. **7**, 4701 (2016).

[40] C. La-o vorakiat, H. Xia, J. Kadro, T. Salim, D. Zhao, T. Ahmed, Y. M. Lam, J.-X. Zhu, R. A. Marcus, M.-E. Michel-Beyerle, and E. E. M. Chia, J. Phys. Chem. Lett. **7**, 1 (2016).

[41] M. Nagai, T. Tomioka, M. Ashida, M. Hoyano, R. Akashi, Y. Yamada, T. Aharen, and Y. Kanemitsu, Phys. Rev. Lett. **121**, 145506 (2018).

[42] H. Wang, L. Valkunas, T. Cao, L. Whittaker-Brooks, and G. R. Fleming, J. Phys. Chem. Lett. **7**, 3284 (2016).

[43] T. Ghosh, S. Aharon, L. Etgar, and S. Ruhman, J. Am. Chem. Soc. **139**, 18262 (2017).

[44] C. Fei, J. S. Sarmiento, and H. Wang, J. Phys. Chem. C **122**, 17035 (2018).

[45] G. Batignani, G. Fumero, A. R. Srimath Kandada, G. Cerullo, M. Gandini, C. Ferrante, A. Petrozza, and T. Scopigno, Nat. Commun. **9**, 1971 (2018).

[46] D. M. Monahan, L. Guo, J. Lin, L. Dou, P. Yang, and G. R. Fleming, J. Phys. Chem. Lett. **8**, 3211 (2017).

[47] P. J. Guo, Y. Xia, J. Gong, D. Y. H. Cao, X. T. Li, X. Li, Q. Zhang, C. C. Stoumpos, M. S. Kirschner, H. D. Wen, V. B. Prakapenka, J. B. Ketterson, A. B. F. Martinson, T. Xu, M. G. Kanatzidis, M. K. Y. Chan, and R. D. Schaller, Adv. Funct. Mater. **30**, 1907982 (2020).

[48] H. Kim, J. Hunger, E. Canovas, M. Karakus, Z. Mics, M. Grechko, D. Turchinovich, S. H. Parekh, and M. Bonn, Nat. Commun. **8**, 687 (2017).

[49] D. Cheng, Z. Liu, L. Luo, C. Vaswani, J. M. Park, Y. Yao, Z. Song, C. Huang, D. H. Mudiyanselage, R. H. J. Kim, Y. Yan, K. M. Ho, and J. Wang, J. Chem. Phys. **151**, 244706 (2019).

[50] Z. Liu, C. Vaswani, X. Yang, X. Zhao, Y. Yao, Z. Song, D. Cheng, Y. Shi, L. Luo, D. H. Mudiyanselage, C. Huang, J. M. Park, R. H. J. Kim, J. Zhao, Y. Yan, K. M. Ho, and J. Wang, Phys. Rev. Lett. **124**, 157401 (2020).

[51] N. Tripathi, M. Yanagida, Y. Shirai, T. Masuda, L. Han, and K. Miyano, J. Mater. Chem. A **3**, 12081 (2015).

[52] D. B. Khadka, Y. Shirai, M. Yanagida, T. Masuda, and K. Miyano, Sustain. Energy Fuels **1**, 755 (2017).

[53] See Supplemental Material at http://link.aps.org/supplemental/10.1103/PhysRevMaterials.5.105402 for the preparation and characterization of the polycrystalline MAPbI$_3$ sample, the TR-OKE detection method, the Raman spectrum of the polycrystalline MAPbI$_3$, the TR-OKE signal of a single-crystal MAPbI$_3$, the experimental initial phases of the coherent phonons, the phonon calculation results without lattice relaxation, the decomposition of the atomic displacements, and the Raman intensity calculations, which includes Refs. [79–81].

[54] K. Ishioka, B. G. Barker, M. Yanagida, Y. Shirai, and K. Miyano, J. Phys. Chem. Lett. **8**, 3902 (2017).

[55] Y. Kanemitsu and T. Handa, Jpn. J. Appl. Phys. **57**, 090101 (2018).

[56] M. A. Perez-Osorio, R. L. Milot, M. R. Filip, J. B. Patel, L. M. Herz, M. B. Johnston, and F. Giustino, J. Phys. Chem. C **119**, 25703 (2015).

[57] S. Ponce, M. Schlipf, and F. Giustino, ACS Energy Lett. **4**, 456 (2019).

[58] M. Park, N. Kornienko, S. E. Reyes-Lillo, M. Lai, J. B. Neaton, P. Yang, and R. A. Mathies, Nano Lett. **17**, 4151 (2017).

[59] A. Mattoni, A. Filippetti, M. I. Saba, C. Caddeo, and P. Delugas, J. Phys. Chem. Lett. **7**, 529 (2016).

[60] M. A. Perez-Osorio, A. Champagne, M. Zacharias, G.-M. Rignanese, and F. Giustino, J. Phys. Chem. C **121**, 18459 (2017).

[61] H. J. Zeiger, J. Vidal, T. K. Cheng, E. P. Ippen, G. Dresselhaus, and M. S. Dresselhaus, Phys. Rev. B **45**, 768 (1992).

[62] M. B. Price, J. Butkus, T. C. Jellicoe, A. Sadhanala, A. Briane, J. E. Halpert, K. Broch, J. M. Hodgkiss, R. H. Friend, and F. Deschler, Nat. Commun. **6**, 8420 (2015).

[63] G. Kresse and J. Furthmüller, Phys. Rev. B **54**, 11169 (1996).

[64] P. E. Blöchl, Phys. Rev. B **50**, 17953 (1994).

[65] G. Kresse and D. Joubert, Phys. Rev. B **59**, 1758 (1999).

[66] F. Lehmann, A. Franz, D. Többens, S. Levcenco, T. Unold, A. Taubert, and S. Schorr, RSC Adv. **9**, 11151 (2019).

[67] Hybrid perovskites, https://github.com/WMD-group/hybrid-perovskites.

[68] J. P. Perdew, A. Ruzsinszky, G. I. Csonka, O. A. Vydrov, G. E. Scuseria, L. A. Constantin, X. Zhou, and K. Burke, Phys. Rev. Lett. **100**, 136406 (2008).

[69] T. Tadano, Y. Gohda, and S. Tsuneyuki, J. Phys.: Condens. Matter **26**, 225402 (2014).

[70] L. Dhar, J. Rogers, and K. Nelson, Chem. Rev. **94**, 157 (1994).

[71] R. Merlin, Solid State Commun. **102**, 207 (1997).

[72] D. Porezag and M. R. Pederson, Phys. Rev. B **54**, 7830 (1996).

[73] J. M. Skelton, L. A. Burton, A. J. Jackson, F. Oba, S. C. Parker, and A. Walsh, Phys. Chem. Chem. Phys. **19**, 12452 (2017).

[74] D. J. Hooton, Philos. Mag. **3**, 49 (1958).

[75] T. Tadano and S. Tsuneyuki, Phys. Rev. B **92**, 054301 (2015).

[76] T. Tadano and S. Tsuneyuki, Phys. Rev. Lett. **120**, 105901 (2018).

[77] I. Errea, Eur. Phys. J. B **89**, 237 (2016).

[78] T. Tadano and S. Tsuneyuki, J. Phys. Soc. Jpn. **87**, 041015 (2018).

[79] M. I. Saidaminov, A. L. Abdelhady, B. Murali, E. Alarousu, V. M. Burlakov, W. Peng, I. Dursun, L. Wang, Y. He, G. Maculan, A. Goriely, T. Wu, O. F. Mohammed, and O. M. Bakr, Nat. Commun. **6**, 7586 (2015).

[80] Y. Liu, Z. Yang, D. Cui, X. Ren, J. Sun, X. Liu, J. Zhang, Q. Wei, H. Fan, F. Yu, X. Zhang, C. Zhao, and S. Liu, Adv. Mater. **27**, 5176 (2015).

[81] Q. Chen, N. De Marco, Y. Yang, T.-B. Song, C.-C. Chen, H. Zhao, Z. Hong, H. Zhou, and Y. Yang, Nano Today **10**, 355 (2015).